The Journal of Chemical Physics ARTICLE pubs.aip.org/aip/jcp

# Existence of a maximum flow rate in electro-osmotic systems

Cite as: J. Chem. Phys. 161, 194502 (2024); doi: 10.1063/5.0231610
Submitted: 1 August 2024 • Accepted: 3 November 2024 •
Published Online: 18 November 2024



Sleeba Varghese,[1] B. D. Todd,[2] and J. S. Hansen[3,a)]

## AFFILIATIONS

[1] CNRS, Physicochimie des Électrolytes et Nanosystèmes Interfaciaux, UMR 8234 PHENIX, Sorbonne Université, Paris, France
[2] Department of Mathematics, School of Science, Computing and Engineering Technologies, Swinburne University of Technology, Melbourne, Victoria 3122, Australia
[3] "Glass and Time," IMFUFA, Department of Science and Environment, Roskilde University, Roskilde 4000, Denmark

[a)] **Author to whom correspondence should be addressed:** jschmidt@ruc.dk

## ABSTRACT

In this work, we investigate the effect of the hydrodynamic wall–fluid friction in electro-osmotic flows. First, we present the solution to the electro-hydrodynamic equation for the electro-osmotic velocity profile, which is derived for an ionic system composed of cations immersed in uncharged solvent particles. The system (solution and walls) is kept electrically neutral using negatively charged walls and will here be referred to as a "counterion-only" system. The theory predicts the existence of a counterion concentration that results in maximum electro-osmotic flow rate, but only if the wall–fluid friction, or equivalently the slip length, is correlated with the system electrostatic screening length. Through equilibrium molecular dynamics simulations, we precisely determine the hydrodynamic slip from the wall–fluid friction, and then, this is used as input to the theoretical predictions. Comparison between the theory and independent non-equilibrium molecular dynamics simulation data confirms the existence of the maximum. In addition, we find that standard hydrodynamic theory quantitatively agrees with the simulation results for charged nanoscale systems for sufficiently small charge densities and ion charges, if the correct slip boundaries are applied.





## I. INTRODUCTION

Efficient fluid transport forms a critical component in the design of any micro or nanoscale fluidic system and has direct implications in a wide array of fields, such as drug delivery, water desalination, pumping, and energy storage.[1–5] In contrast to macroscale systems, conventional pressure-driven flow at the nanoscale is often impossible to achieve for practical applications due to the extremely high pressure gradient required to generate a net fluid flow inside the nanochannel.[6] Hence, viable alternatives to pressure-driven flow have to be considered to transport fluid for nanoscale systems. Among various methods, electro-osmotic flow (EOF) has shown great promise in being an energy-efficient way to transport the fluid through nanoconfined systems,[7] and thus understanding electro-osmotic flow behavior at the nanoscale can help in the efficient design of miniature devices.

Modeling electro-osmotic flows through nanochannels is often mathematically challenging because the classical assumptions usually employed in continuum theories may not capture the fluid behavior close to the walls. For example, the classical Poisson–Boltzmann (PB) equation cannot predict the ionic layering observed in the wall–fluid interfacial region, which can become highly influential when the channel size measures only a few nanometers.[8] Another approximation that also requires serious consideration when studying nanoscale EOFs is the reliability of the no-slip boundary condition at the walls. Experimental and simulation studies have shown that the no-slip boundary condition usually employed in macroscale flows becomes insufficient to describe the hydrodynamics in nanochannels.[6,9–11] Hence, at the nanoscale, it becomes essential to incorporate the fluid–solid interfacial slip in the theoretical prediction of the electro-osmotic velocity profile.

Previous studies have addressed the inadequacies in the prediction of EOF in nanochannels by introducing modifications to the classical PB equation and coupling with the hydrodynamics.[8,12,13] Even though appreciable progress has been made in modeling the electrostatics part in nanoconfined charged systems, precise

and independent calculation of the hydrodynamic slip at the fluid–solid interface of a charged system still remains. Most studies on nanoscale EOF have quantified the hydrodynamic slip using the parameter known as slip length.[12,14–19] This is often calculated from the velocity profile generated from nonequilibrium molecular dynamics (NEMD) simulations. Even though NEMD simulations can provide an estimate for the effective slip for simple systems, this method of slip estimation does have some serious limitations. First, the slip length calculated from NEMD simulations should be independent of the applied external driving field to mimic typical experimental conditions. This requires performing several simulations at different and sufficiently low field strengths to determine the field-independent slip length, which can be a computationally intensive procedure.[20] Second, for high slip systems, it has been shown that small uncertainties in the velocity profile can lead to large changes in the slip length,[21] making the calculation of a precise value for hydrodynamic slip in this way highly questionable.

Here, the EOF is investigated for an ionic solution with only a single type of dissolved ion confined between walls that have an opposite charge to the ion. Such a system is often referred to as a "counterion-only" system due to the absence of co-ions.[22] The system corresponds to a salt-free solution with charged walls and can be used to model realistic situations, such as water flow through lipid bilayers, clay sheets, or along surfaces with ionizable sites, and also in the case of lamellar liquid crystals.[22,23] The hydrodynamic slip is quantified using the interfacial friction coefficient (also known as the Navier friction coefficient), which, to overcome the problems with NEMD estimates mentioned above, is computed from the equilibrium molecular dynamics simulations using the methodology proposed in the works of Hansen *et al.*[24] and Varghese *et al.*[25] To understand the effect of coupling between electrostatics and hydrodynamic slip, we derive an approximate analytical solution for the volumetric flow rate of a counterion-only system. We find that there exists an optimal counterion concentration that can result in a maximum electro-osmotic flow rate in the case of non-wetting nanochannels. This is confirmed by the NEMD simulations.

## II. THEORY

We start our theoretical treatment from the Poisson–Boltzmann (PB) equation for a counterion-only system. For a nanoslit pore with confinement along the $z$ axis, as shown in Fig. 1, the one-dimensional form of the PB equation is given as[26]

$$\frac{d^2\psi}{dz^2} = -\frac{q\rho_0}{\varepsilon} e^{-q\psi/k_BT}, \tag{1}$$

where $z$ is the spatial coordinate, and we choose the coordinate system such that $z = 0$ is the midpoint of the channel. Here, $\psi$ is the electric potential; $\rho_0$ is the reference ion number density, where the electric potential becomes zero; $q$ is the charge of the ions; $k_B$ is the Boltzmann constant; $T$ is the system temperature; and $\varepsilon = \varepsilon_0\varepsilon_r$, where $\varepsilon_0$ and $\varepsilon_r$ are the vacuum permittivity and relative permittivity, respectively. We will assume that the charge dependency of $\varepsilon$ can be ignored. It should be noted that the channel height, $H$, is the distance between the center of mass of the inner-most wall layers minus the hydrodynamic stationary (stagnant) Stern layer if this is present.

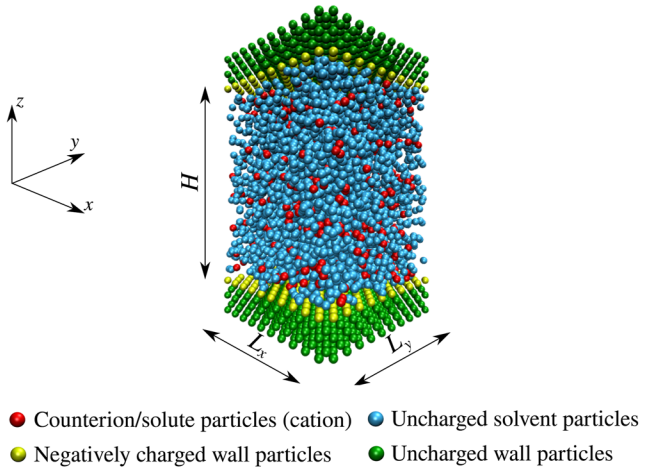


**FIG. 1.** Molecular representation of the charged system used in this study. The walls are placed in the $x$–$y$ plane with a wall area equal to $L_x \times L_y$. The channel height, $H$, is defined as the available channel height for the mobile ions; this is estimated from the density and velocity flow profiles.

An analytical solution exists for Eq. (1) and is given by[22]

$$\psi(z) = \frac{k_BT}{q} \ln\left(\cos^2(z/\lambda)\right), \tag{2}$$

where $\lambda$ is the screening length parameter,

$$\lambda = \sqrt{\frac{2\varepsilon k_BT}{q^2\rho_0}}. \tag{3}$$

From the solution, Eq. (2), we can see that the reference electric potential is $\psi = 0$ at $z = 0$, such that $\rho_0$ corresponds to the counterion concentration at the channel center, that is, $\rho_0 = \rho(0)$. Importantly, enforcing continuity on the solution in Eq. (2), there exists a lower bound $0 < \cos^2(z/\lambda)$ implying that if we define the half-height $h = H/2$, we have the constraint $\lambda > 2h/\pi$ since $-\pi/2 < z/\lambda < \pi/2$ and $-h \le z \le h$. This means that Eq. (2) is only valid for sufficiently large screening lengths; this is true in the Debye–Hückel limit $k_BT \gg q^2\rho_0$.

Now, using Eq. (2) and the Boltzmann distribution for counterions, $\rho(z) = \rho_0 e^{-q\psi(z)/k_BT}$, we obtain the counterion concentration profile in terms of the screening length and reference concentration,

$$\rho(z) = \frac{\rho_0}{\cos^2(z/\lambda)}. \tag{4}$$

Applying the charge neutrality condition, we have the relation,

$$-2\Sigma_{\text{wall}} = \int_{-h}^{h} q\rho(z)dz, \tag{5}$$

where $\Sigma_{\text{wall}}$ is the surface charge density of one wall. Substituting Eq. (4) in Eq. (5) we can get a relation between the screening length and surface charge density of the wall as

$$\frac{2k_BT}{q\lambda}\tan(h/\lambda) = -\frac{\Sigma_{\text{wall}}}{\varepsilon}. \tag{6}$$

Equation (6) can be further simplified using Eq. (3) to the form

$$\lambda\tan(h/\lambda) = -\frac{\Sigma_{\text{wall}}}{q\rho_0}. \tag{7}$$

Since we do not explicitly compute the permittivity, we apply Eq. (7) to calculate $\lambda$ using the Newton–Raphson algorithm,[27] with $\rho_0$ as an input parameter from molecular dynamics simulations.

Once the ion concentration distribution is known, we can write the Navier–Stokes equation for the EOF. For low Reynolds number and in the steady-state, this is[6,26]

$$\eta_0\frac{d^2u_x}{dz^2} = -q\rho E_x, \tag{8}$$

where $u_x$ is the $x$-component of the velocity, $\eta_0$ is the shear viscosity, and $E_x$ is the external electric field applied in the $x$-direction. We assume that $\eta_0$ is independent of the charge concentration. Substitution of Eq. (4) in Eq. (8) leads to

$$\frac{d^2u_x}{dz^2} = -\frac{q\rho_0\,E_x}{\eta_0\cos^2(z/\lambda)}, \tag{9}$$

and integrating yields

$$u_x(z) = \frac{q\rho_0\lambda^2E_x}{\eta_0}\ln(\cos(z/\lambda))\,E_x + D_1z + D_2, \tag{10}$$

where $D_1$ and $D_2$ are constants of integration. We use the system symmetry and slip boundary conditions, i.e.,

$$u_x(-h) = u_x(h) = u_s, \tag{11}$$

where $u_s$ is the slip velocity, and we arrive at the solution for the velocity profile,

$$u_x(z) = \frac{q\rho_0\lambda^2E_x}{\eta_0}\ln\left[\frac{\cos(z/\lambda)}{\cos(h/\lambda)}\right] + u_s. \tag{12}$$

We wish to express the slip velocity in terms of the slip-length, $L_s$. From the continuity of the shear pressure (or stress) at the interface between the mobile fluid and stagnant surface, we have[6]

$$u_s = \frac{\eta_0}{\xi_0}\frac{du_x(z)}{dz}\bigg|_{z=\pm h} = \frac{q\rho_0\lambda E_x\,\tan(h/\lambda)}{\xi_0}, \tag{13}$$

where $\xi_0$ is the interfacial friction coefficient. It should be noted that Eq. (13) is the Navier-slip boundary condition, which is simply a Neumann boundary. By combining Eqs. (12) and (13), we can write the EOF velocity in the final form

$$u_x(z) = \frac{q\rho_0\lambda^2E_x}{\eta_0}\left(\ln\left[\frac{\cos(z/\lambda)}{\cos(h/\lambda)}\right] + \frac{L_s\tan(h/\lambda)}{\lambda}\right), \tag{14}$$

where $L_s = \eta_0/\xi_0$ is the slip length. Equation (14) represents an electro-hydrodynamic model for the velocity profile, where the second term on the right-hand side describes the effect of the hydrodynamic slip.

The flow can be quantified by the volumetric flow rate, $Q$, through a cross section of the pore, $[-h,h]\times[-w,w]$, by

$$Q = \int_{-w}^{w}dy\int_{-h}^{h}u_x(z)\,dz = 2w\int_{-h}^{h}u_x(z)\,dz. \tag{15}$$

To our knowledge, the integral does not have a known solution of elementary functions, and therefore, we Taylor expand around the channel center, $z = 0$, approximating $\ln|\cos(z/\lambda)| \approx -z^2/(2\lambda^2)$. Equation (15) is then

$$Q \approx -\frac{2q\rho_0\lambda^2E_x}{\eta_0}\left[\frac{h^3}{3\lambda^2} + 2h\ln(\cos(h/\lambda)) - \frac{2L_sh}{\lambda}\tan(h/\lambda)\right]. \tag{16}$$

First, we consider the flow rate in the special case of no-slip, $L_s = 0$. We then investigate the flow rate dependency of the screening length, $Q = Q(\lambda)$. Since we have the relation,

$$-\frac{d}{d\lambda}\left(\frac{h^3}{3\lambda^2} + 2h\ln(\cos(h/\lambda))\right) = \frac{2}{3}\left(\frac{h}{\lambda}\right)^3 - 2\left(\frac{h}{\lambda}\right)^2\tan(h/\lambda) < 0 \tag{17}$$

for $2h/\pi < \lambda < \infty$, we see that the flow rate decreases monotonically with screening length, thus, the maximum flow rate is obtained in the limit $\lambda \to 2h/\pi$ for zero slip.

Now, consider the case where the slip length is non-zero. One must expect that the slip length depends on the detailed ion layering in the wall–fluid interface region. This, in turn, depends on the ion concentration or equivalently the screening length, and therefore, we have a correlation between the slip length and the screening length, $L_s = L_s(\lambda)$. By differentiation of Eq. (16), we then get the implicit equation for the possible maximum flow rate at $\lambda = \lambda_{\max}$,

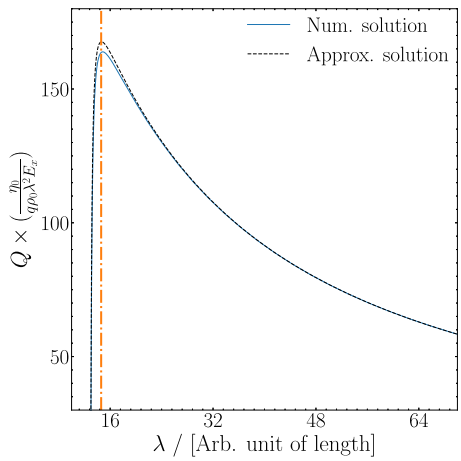


**FIG. 2.** Volumetric flow rate, $Q$, as a function of screening length, $\lambda$, using the correlation function $L_s = \alpha\lambda - \beta$. In arbitrary units, we have applied variable values $h = 20$, $\alpha = 6$, $\beta = 13\alpha + 1 = 79$, and $13 \le \lambda \le 100$. The vertical line indicates the value for $\lambda_{\max}$ obtained from Eq. (18).

$$\frac{2}{3}\left(\frac{h}{\lambda_{\max}}\right)^3 - \frac{2h}{\lambda_{\max}}\left(\frac{L_s + h}{\lambda_{\max}} - L_s'(\lambda_{\max})\right)\tan\left(h/\lambda_{\max}\right) - \frac{2h^2 L_s(\lambda_{\max})}{\lambda_{\max}^3}\sec^2\left(h/\lambda_{\max}\right) = 0. \tag{18}$$

The correlation function is unknown *a priori*. As a simple example, which will later be confirmed by the simulation data, we here choose the form $L_s = \alpha\lambda - \beta$, where $\alpha > 0$, $\lambda > 2h/\pi$ (by the constraint discussed above), and $\beta$ is chosen such that $L_s \geq 0$, that is, $\beta \leq \alpha\lambda$. Figure 2 shows the volumetric flow rate for this choice of correlation function: the full line is the result obtained from direct numerical integration of Eq. (14), and the dashed line is from the approximation in Eq. (16). We see that $Q$ indeed features a maximum at $\lambda_{\max} \approx 14.6$ (in some arbitrary unit) as predicted by Eq. (18) (vertical line); here, a standard minimization algorithm is used to find the value for $\lambda_{\max}$.[28]

## III. MOLECULAR DYNAMICS SIMULATIONS

Molecular dynamics simulations were performed using the Large-scale Atomic/Molecular Massively Parallel Simulator (LAMMPS) package.[29] All particles (both fluid and wall) in the system were modeled as simple spherical particles that interact pairwise via the Lennard-Jones (LJ) potential,

$$\phi(r) = \begin{cases} 4\varepsilon\left[\left(\frac{\sigma}{r}\right)^{12} - C\left(\frac{\sigma}{r}\right)^{6}\right] & \text{if } r \leq r_c, \\ 0 & \text{if } r > r_c, \end{cases} \tag{19}$$

where $\sigma$ and $\varepsilon$ are the LJ parameters defining the simulation characteristic length and energy scales, respectively. In addition, $r$ is the interatomic distance between the atoms, and $r_c$ is the interaction cutoff, which is kept at $2.5\sigma$. $C$ is the wetting coefficient that controls the different wall–fluid wetting properties; we used a fluid–fluid wetting coefficient of $C = 1.2$, and for the wall–fluid, we used $C = 0.5$. These values of wetting coefficients were previously shown to model a non-wetting interface.[30] Notice that Eq. (19) can also be written in the form of the standard LJ potential, such that the wetting is controlled by the LJ parameters, $\sigma$ and $\varepsilon$.[31] All particles have the same mass, $m$, and the mechanical properties can be expressed in terms of $\sigma$, $\varepsilon$, and $m$. As it is common practice, we will from hereon, set the parameters to unity and omit these units and the units relating to the electrostatics.

The short-range Coulombic interactions were calculated using an interaction cutoff of $r_c = 2.5$, and for the long-ranged interactions, the Ewald algorithm is used with the particle–particle-particle–mesh solver of LAMMPS[29,32,33] with a relative root mean square error in the per-atom force calculations below $1 \times 10^{-4}$. To accommodate the non-periodicity in the $z$-direction, we used the corrected Ewald algorithm EW3DC,[33] where the ratio of extended volume to actual channel size is set as 3.0.

We studied systems with two different ion charges, $q = +0.2$ and $q = +1.6$, and with varying ion concentrations. All systems have the same overall fluid density of 0.9. Tables I and II present the different system properties for $q = +0.2$ and $q = +1.6$, respectively; all quantities are given in LJ units as mentioned above; however, it is important to note that for a typical value for the length scale, say $\sigma = 0.5$ nm, the molarity of the systems ranges from 0.08M to 7M, that is, the concentration range falls within realistic values.

**TABLE I.** Summary of the calculated system properties for ion charge $q = +0.2$. $\rho_0$ is the ion density at $z = 0$; $\lambda$ is the screening length; $\xi_0$ the friction coefficient; and $Q$ the measured flow rate from the NEMD simulations. Except for $Q$, all properties are calculated from EMD simulations. $h = H/2$ is estimated to be 9.7 for all systems. Notice that for $x = 0.61$, the friction coefficient cannot be calculated, and therefore, we do not estimate other system properties.

| $x$ | $\rho_0$ | $\lambda$ | $\xi_0$ | $\Sigma_{\text{wall}}$ | $Q$ (NEMD) |
|---|---|---|---|---|---|
| 0.007 | 0.006 | 28.92 | $1.27 \pm 0.03$ | −0.0125 | $0.4 \pm 0.3$ |
| 0.014 | 0.011 | 17.26 | $1.25 \pm 0.03$ | −0.025 | $0.7 \pm 0.2$ |
| 0.049 | 0.036 | 12.72 | $1.30 \pm 0.03$ | −0.0875 | $3.1 \pm 0.3$ |
| 0.11 | 0.064 | 9.55 | $1.35 \pm 0.03$ | −0.2 | $6.2 \pm 0.2$ |
| 0.22 | 0.098 | 8.15 | $1.78 \pm 0.05$ | −0.4 | $10.3 \pm 0.2$ |
| 0.33 | 0.122 | 7.14 | $2.45 \pm 0.07$ | −0.6 | $12.0 \pm 0.2$ |
| 0.39 | 0.133 | 7.51 | $3.08 \pm 0.07$ | −0.7 | $12.2 \pm 0.2$ |
| 0.50 | 0.166 | 7.45 | $5.43 \pm 0.13$ | −0.9 | $12.1 \pm 0.2$ |
| 0.61 | ⋯ | ⋯ | ⋯ | ⋯ | $7.1 \pm 0.3$ |

The walls were placed in the $x$–$y$ plane, with periodicity in both directions and symmetry about the channel center, $z = 0$. Each wall consists of five layers of atoms arranged in a face-centered cubic lattice with a density of 1.0 and an interlayer distance of 0.8. The wall particles were maintained around their initial equilibrium positions $\mathbf{r}_{\text{eq}}$, using a harmonic potential given by $\phi_s = \frac{1}{2}k_s(\mathbf{r}_i - \mathbf{r}_{\text{eq}})^2$, where $k_s = 150$ is the spring constant and $\mathbf{r}_i$ is the instantaneous position of the wall particle.[34] The inner-most layer of each wall was negatively charged to maintain electroneutrality for the system, with the total charge on each wall being $-qN_{\text{ci}}/2$, where $N_{\text{ci}}$ is the total number of counterions in the system; see Table I. The wall area in the $x$–$y$ plane is $L_x \times L_y = 16 \times 16 = 256$, where $L_x$ and $L_y$ are the simulation box dimensions along the $x$ and $y$ axes, respectively. Figure 1 shows a snapshot of the system.

Equilibrium molecular dynamics (EMD) simulations for each system were performed for $3 \times 10^6$ steps in total, where the initial $2 \times 10^6$ steps were used to equilibrate the system at $T = 1.0$ by thermostating the walls using a Nosé–Hoover[35,36] thermostat. The final $1 \times 10^6$ steps were used to collect data for post-processing. The equations of motion for all particles were integrated using the velocity-Verlet[37] scheme with an integration time step $\Delta t = 0.001$. 20 independent EMD simulations were performed for each system to obtain sufficient statistics.

**TABLE II.** Summary of the system properties with ion charge $q = +1.6$. The symbols are the same as presented in Table I and again $h = 9.7$.

| $x$ | $\rho_0$ | $\lambda$ | $\xi_0$ | $\Sigma_{\text{wall}}$ | $Q$ (NEMD) |
|---|---|---|---|---|---|
| 0.014 | 0.0016 | 6.59 | $1.46 \pm 0.07$ | −0.2 | $3.8 \pm 0.2$ |
| 0.028 | 0.0017 | 6.42 | $1.81 \pm 0.05$ | −0.4 | $5.6 \pm 0.2$ |
| 0.042 | 0.0018 | 6.36 | $2.72 \pm 0.10$ | −0.6 | $5.3 \pm 0.2$ |
| 0.049 | 0.0016 | 6.33 | $3.44 \pm 0.10$ | −0.7 | $5.1 \pm 0.2$ |
| 0.062 | 0.0015 | 6.31 | $5.87 \pm 0.20$ | −0.9 | $3.9 \pm 0.2$ |

We also performed nonequilibrium molecular dynamics (NEMD) simulations to investigate the EOF for each system. Each NEMD simulation was performed for a total of $4 \times 10^6$ steps, with the initial $2 \times 10^6$ steps used for equilibration of the system at $T = 1.0$, by thermostating the walls using the Nosé–Hoover[35,36] thermostat. After the initial equilibration, an external electric field with magnitude $E_x = 0.075$ was applied for $2 \times 10^6$ steps to achieve a steady flow. The data were collected from the final $1 \times 10^6$ steps of the non-equilibrium run. Every NEMD result was also averaged across 20 independent simulations.

## IV. RESULTS AND DISCUSSION

First, we focus on the case with ion charge $q = +0.2$. Figure 3 shows the EMD ion distribution (or profiles) predicted by Eq. (4) (dashed line) and that obtained from the simulations (full line). In this comparison, the value for $\rho_0$ is determined directly from the simulations, and the screening length is calculated numerically from the relation in Eq. (7); see values presented in Table I. Since the statistical uncertainty associated with $\rho_0$ is negligible, we do not consider the propagation of this statistical uncertainty in our computation of $\lambda$.

Recall, that here, the channel width is defined to be the part of the channel which is available to the mobile fluid particles. From the density profile, we estimate $H \approx 19.4$; this value is independent of whether the external force is applied or not. Since $h = H/2$ enters the expression for the EOF velocity profile, the predicted profile and flow rate will indeed depend on this estimate. The authors are not aware of an unambiguous definition.[6]

Clearly, Eq. (4) does not capture the layering of the counterions close to the walls, but for sufficiently small ion concentrations, it shows satisfactory prediction for the density in the bulk region of the channel. The external force density that drives the flow, $q\rho E_x$, will vary strongly in the wall–fluid region and is, therefore, not correctly modeled by Eq. (4). Recently, it has been shown that incorporating the coupling between the solvent density and ion density into the PB theory, one can successfully model the layering, at least for low counterion concentrations.[12,13] It is not the purpose here to pursue this coupling effect, but we will comment on the point in the following.

To quantify the hydrodynamic slip, we compute the interfacial friction coefficient, $\xi_0$, using the equilibrium method proposed by Varghese *et al.*,[25] which is a statistical improvement of the method devised by Hansen *et al.*[24] In the supplementary material, it is shown how it is applied in this particular case of a charged system. Table I presents the friction coefficients for charge $q = +0.2$; we observe that increasing the ion concentration increases hydrodynamic friction between the wall and fluid particles, concurring with the results reported in previous studies.[13,38] We also find that the method becomes unreliable above mole fractions $x > 0.5$; the exact reason for this limitation is not clear; however, we expect it to be due to the emergence of crystallization in the interfacial region, leading to unrealistic values for interfacial friction.

From $\xi_0$, the slip length, $L_s$, can be found using the definition $L_s = \eta_0/\xi_0$. To this end, we have performed a series of NEMD simulations in order to investigate the viscosity dependence of the ion concentration (see the supplementary material), and we conclude that the viscosity does not vary significantly in the

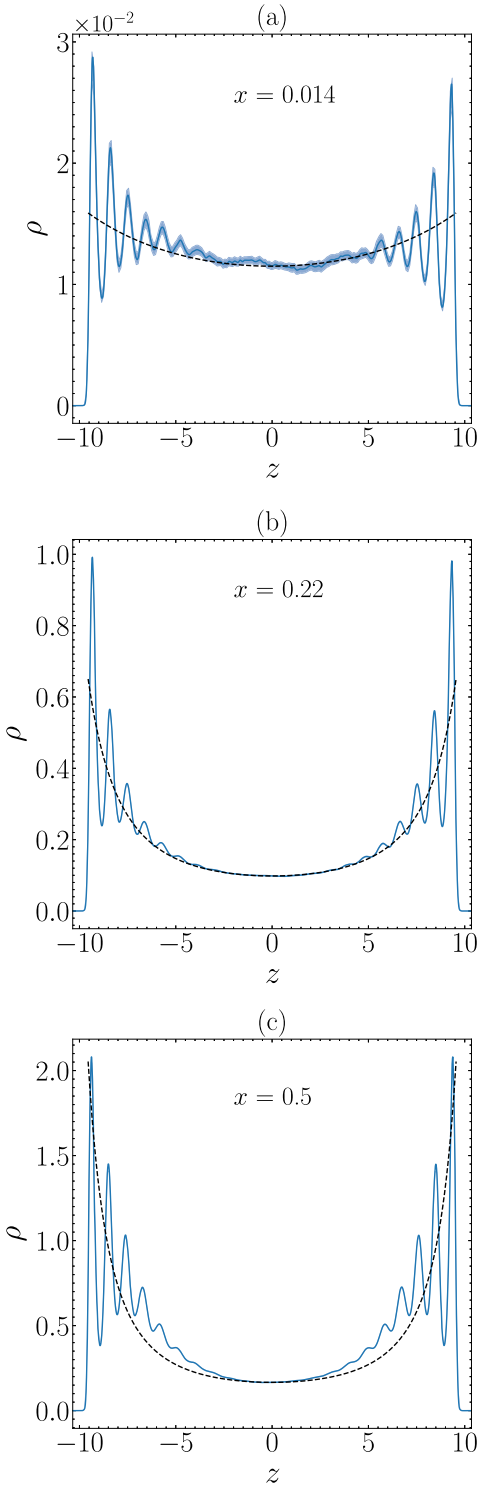


**FIG. 3.** Variation of the counterion density $\rho$ for different counterion mole fractions across the channel width. The solid lines represent the density profile obtained from EMD simulations, and the dashed lines represent the density profile predicted by Eq. (4). The shaded region in panel (a) corresponds to the statistical error associated with the data.

concentration range studied here. This also validates the assumption in the theory section. Therefore, the viscosity equals, within the standard deviation, the (non-charged solvent only) case viscosity $\eta_0 = 4.1 \pm 0.1$.

Next, we compare the velocity profiles obtained in the simulations with the predicted profiles, as shown in Fig. 4, using the parameter values presented in Table I; that is, in the predictions, we do not perform any fitting to the NEMD profiles. It should be noted that we have excluded predictions from the highest concentration, $x = 0.61$, since the friction coefficient was not determined for this system.

For $x = 0.014$, the noise-to-signal ratio is very large in the simulation data and the profile curvature is not clearly visible. Due to these large statistical uncertainties, the direct comparison is inconclusive for low concentrations. For intermediate concentrations, as shown in Fig. 4(b), the standard theory agrees very well with the simulation data when the slip boundary is applied. We again highlight that no direct fitting is carried out in comparison. There is no observable effect of the ion layering on the flow profile in the wall–fluid region. This phenomenon is equivalent to what is seen in the standard Poiseuille flow, where the flow profile is unaffected by the density layering for sufficiently large channels due to the nonlocal fluid response.[6,39] Therefore, even if the external driving force is given by the charge density, the small-scale variation has no effect on the flow profile. For large ion concentrations, as shown in Fig. 4(c), one clearly sees that the ion layering affects the flow in the wall–fluid region. The fluid in the region is not stagnant, hence, it does not form a Stern layer; however, the strain rate is reduced compared to the predictions indicating a reduced shear stress in the wall–fluid region.

Figure 5 shows the volumetric flow rate obtained from the simulations and the predicted flow rate, Eq. (16), using both zero and non-zero slip. The simulation flow rates are calculated directly from Eq. (15) using $w = 8$ and the velocity profiles from simulations. While Eq. (16) overestimates the flow rate for larger counterion concentrations, the prediction is in excellent agreement with simulation data at lower concentrations.

We note that for $q = +0.2$, the simulation data for the flow rate features a plateau and then drops at $x = 0.61$, thus, the flow rate has a maximum. While the existence of this maximum is predicted by the theory, we cannot make a direct comparison since the method to calculate the friction coefficient fails at high concentrations.

To highlight the effect of the slip, we write the flow rate difference between the slip and the no-slip situations using the last term in Eq. (16),

$$\frac{4hq\rho_0\lambda^2 E_x}{\eta_0}\,\frac{L_s\tan(h/\lambda)}{\lambda} = \frac{4hE_x}{\eta_0}|\Sigma_{\text{wall}}|L_s, \tag{20}$$

where $|\Sigma_{\text{wall}}|$ represents the absolute value of the surface charge density. If $Q_{L_s=0}$ is the flow rate for zero slip, we can define the theoretically predicted enhancement coefficient,[6]

$$E = \frac{Q}{Q_{L_s=0}} = 1 + \frac{4hE_x}{\eta_0 Q_{L_s=0}}|\Sigma_{\text{wall}}|L_s. \tag{21}$$

This enhancement coefficient is shown in the inset of Fig. 5. Notice that the product $|\Sigma_{\text{wall}}|L_s$ determines the flow enhancement, and that the enhancement decreases as a function of concentration due to the

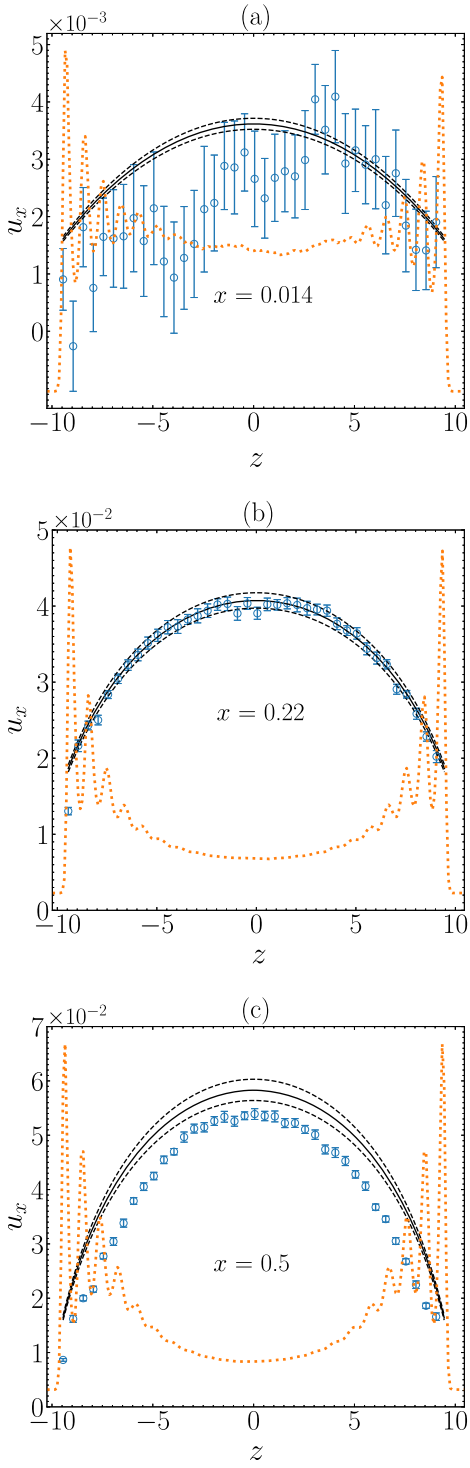


**FIG. 4.** Electro-osmotic velocity profile, $u_x$, for different counterion concentrations. The circles represent the electro-osmotic velocity profile obtained from NEMD simulations. The solid lines represent the electro-osmotic velocity profile predicted using Eq. (14). The dashed lines are the error range for the predicted profiles due to the standard errors in the values for $\eta_0$ and $\xi_0$. The superimposed dotted lines are scaled and shifted counterion density profiles.

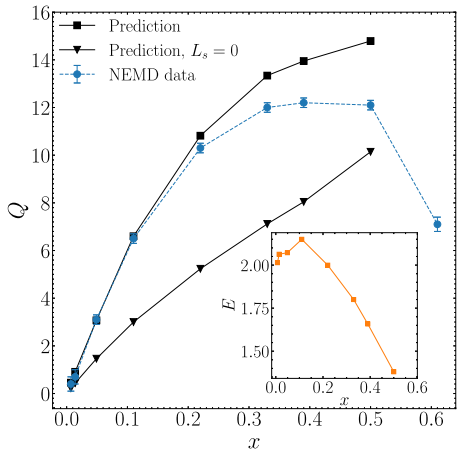


**FIG. 5.** Volumetric flow rate vs counterion concentration for $q = +0.2$. The circles connected with the dashed line are the results from the NEMD simulations; the squares connected with the solid line are the theoretical predictions with slip; and the triangles connected with the solid line are the theoretical predictions with no-slip. The inset shows the variation of the enhancement coefficient, $E$, with counterion concentration.

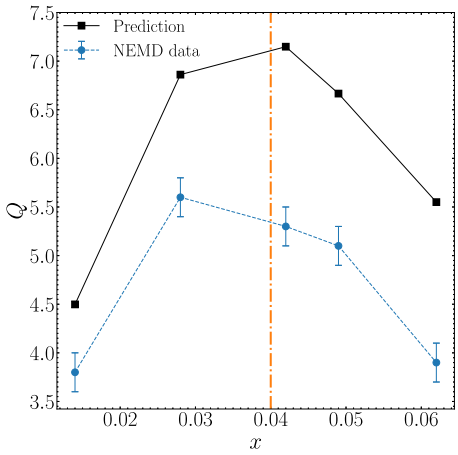


**FIG. 7.** Volumetric flow rate vs counterion concentration for $q = +1.6$. The circles connected with the dashed line are the results from the NEMD simulations, and the squares connected with the solid line are the theoretical predictions. The vertical dashed–dotted line indicates the predicted counterion concentration giving the maximum electro-osmotic flow rate.

increasing friction coefficient (or equivalent to the decreasing slip length).

We now switch to the case where the ion charge is $q = +1.6$; the system properties are presented in Table II. As it is seen directly from the table values, this system features a maximum flow rate in the regime where we can calculate the friction coefficient. To compare the prediction of the maximum with simulation data, Fig. 6 shows the correlation between the slip length $L_s$ and the screening length $\lambda$. For low $\lambda$, corresponding to large ion concentrations, $L_s$ increases linearly with $\lambda$ indicating that in this regime, the wall–fluid interactions (and resulting fluid layering near the wall) are affected by the presence of the ions. As $\lambda$ increases (the concentration decreases), we

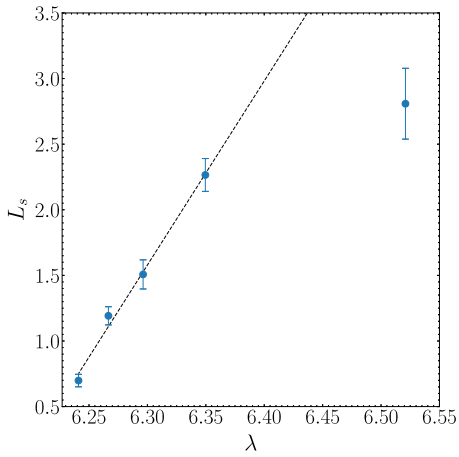


**FIG. 6.** Slip length, $L_s$, vs screening length, $\lambda$, for $q = +1.6$. The circles with error bars are the results derived from EMD simulation data, and the dashed line is a linear fit of the lowest four data points.

can expect the wall–fluid interactions to be dominated by the solvent particle layering; this picture agrees with the observation that the slip length becomes less dependent on the screening length in the low concentration regime.

According to the theory, a maximum flow rate may exist if the slip length is correlated with the screening length. To investigate this, we perform a linear fit to the lowest four data points giving a correlation function $L_s(\lambda) = 14.03\lambda - 86.79$, as shown in Fig. 6. Substitution into Eq. (18), we obtain maximum flow rate at $\lambda_{max} = 6.4$, or equivalently, at concentration $x = 0.04$. This is in good agreement with the data presented in the table.

In Fig. 7, we compare the predicted flow rate and the flow rate obtained from NEMD simulations for $q = +1.6$. While the predictions are in qualitative agreement with the simulation data, the predicted flow rate is overestimated for the systems studied here. If we compare to the case for $q = +0.2$ and at the corresponding wall charges, which is a measure for the overall system charge, one can conclude that the theory performs better for lower ion charge and that, in general, the EOF properties depend on both charge density and ion charge.

The reason for the latter effect is due to the different ion layering at the wall–fluid surface. Figure 8 shows the ion density profiles for $q = +0.2$ and $q = +1.6$ at same system charge $|\Sigma_{wall}| = 0.4$. For $q = +0.2$, this corresponds to the concentration $x = 0.22$, where the velocity predictions are excellent and the bulk ion number density profile follows the PB equation. For $q = +1.6$, the concentration is $x = 0.028$, that is, an order of magnitude lower than for $q = +0.2$ with the same system charge. It can be seen that almost all ions are located in the wall–fluid interface and that the screening length is reduced dramatically compared to the case of $q = +0.2$. For small screening length, the driving force acts primarily in the wall–fluid interface, where the PB equation does not capture the correct distribution and the theory predictions will deviate significantly from the simulation data.

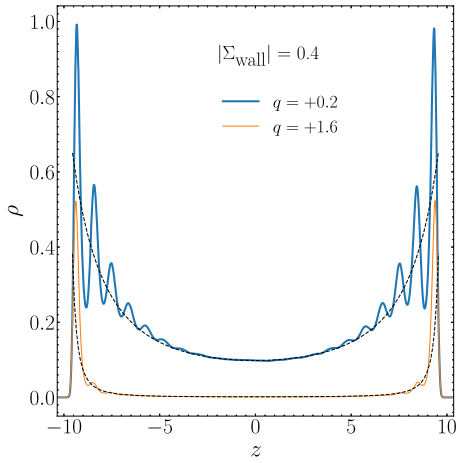


**FIG. 8.** Density profiles for $q = +0.2$ and $q = +1.6$. Both the systems have the same overall charge density $|\Sigma_{wall}| = 0.4$. The full lines are the simulation results and the black dotted lines are the PB equation prediction.

## V. CONCLUSIONS

In summary, we have devised an electro-hydrodynamic description for a counterion-only flow system that correctly incorporates fluid slip and, therefore, enables a correct prediction of the EOF for sufficiently small charge densities and ion charges. The inclusion of slip is based on the independent calculation of the friction coefficient parameter, and the method relies only on the interface particles and we can attribute the friction coefficient to be an intrinsic property of the solid–fluid interface.

The main result of this study is that the EOF features a maximum volumetric flow rate. This is due to the correlation between the slip length and the screening length; the latter itself being dependent on the system ion concentration. In no-slip systems, the flow is monotonically increasing with ion concentration and does not feature this non-trivial maximum. The result was predicted by the continuum theory and confirmed through direct NEMD simulations. This also implies that the continuum theory correctly predicts the flow for sufficiently low charge density, even if the charge density profile does not follow the simple PB predictions. Finally, we also find that the flow properties depend on the charge of the counterion present in the solution.

The result implies that it is possible to tune the electro-osmotic flow in a counterion-only system if we have accurate values for the hydrodynamic slip. A specific application of this could be in improving the efficiency of water flow through nanochannels coated with polyelectrolytes; recent studies on surfaces coated with polyelectrolytes have reported the possibility of maximizing the EOF by controlling the nature of the confining substrate.[40,41] In contrast to the present study, for aqueous solutions, it is important to consider the anisotropic dielectric nature of water under nanoconfinement.[42–44] Hence, to optimize the flow in these aqueous solutions, we will need to understand the influence of dielectric anisotropy on the electro-osmotic behavior of confined systems.

## SUPPLEMENTARY MATERIAL

The supplementary material contains further theoretical details and results relevant to this work. It includes details on the estimation of viscosity and a detailed theoretical description of the friction coefficient methodology employed in this work.

## ACKNOWLEDGMENTS

This work was performed on the OzSTAR national facility at Swinburne University of Technology. The OzSTAR program receives funding in part from the Astronomy National Collaborative Research Infrastructure Strategy (NCRIS) allocation provided by the Australian Government, and from the Victorian Higher Education State Investment Fund (VHESIF) provided by the Victorian Government. The authors thank Professor Peter Daivis for the helpful discussions of our work.

## AUTHOR DECLARATIONS

### Conflict of Interest

The authors have no conflicts to disclose.

### Author Contributions

**Sleeba Varghese**: Conceptualization (equal); Formal analysis (equal); Investigation (lead); Methodology (equal); Project administration (equal); Validation (equal); Writing – original draft (equal). **B. D. Todd**: Conceptualization (equal); Formal analysis (equal); Investigation (supporting); Methodology (equal); Project administration (equal); Supervision (equal); Validation (equal); Writing – original draft (equal). **J. S. Hansen**: Conceptualization (equal); Formal analysis (equal); Investigation (supporting); Methodology (equal); Project administration (equal); Supervision (equal); Validation (equal); Writing – original draft (equal).

## DATA AVAILABILITY

The data that support the findings of this study are available from the corresponding author upon reasonable request.

## REFERENCES

[1] C. M. Lieber, "Nanoscale science and technology: Building a big future from small things," MRS Bull. **28**, 486–491 (2003).
[2] R. F. Service, "Desalination freshens up," Science **313**, 1088–1090 (2006).
[3] S. Ghosh, A. Sood, and N. Kumar, "Carbon nanotube flow sensors," Science **299**, 1042–1044 (2003).
[4] Z. Siwy and A. Fuliński, "Fabrication of a synthetic nanopore ion pump," Phys. Rev. Lett. **89**, 198103 (2002).
[5] X. Zhou, F. Wu, J. Kou, X. Nie, Y. Liu, and H. Lu, "Vibrating-charge-driven water pump controlled by the deformation of the carbon nanotube," J. Phys. Chem. B **117**, 11681–11686 (2013).
[6] J. S. Hansen, *Nanoscale Hydrodynamics of Simple Systems* (Cambridge University Press, 2022).
[7] A. Alizadeh, W.-L. Hsu, M. Wang, and H. Daiguji, "Electroosmotic flow: From microfluidics to nanofluidics," Electrophoresis **42**, 834–868 (2021).

[8]R. Qiao and N. R. Aluru, "Ion concentrations and velocity profiles in nanochannel electroosmotic flows," J. Chem. Phys. **118**, 4692–4701 (2003).
[9]J. S. Hansen, J. C. Dyre, P. J. Daivis, B. D. Todd, and H. Bruus, "Nanoflow hydrodynamics," Phys. Rev. E **84**, 036311 (2011).
[10]J. S. Hansen, J. C. Dyre, P. Daivis, B. D. Todd, and H. Bruus, "Continuum nanofluidics," Langmuir **31**, 13275–13289 (2015).
[11]G. Karniadakis, A. Beskok, and N. Aluru, *Microflows and Nanoflows: Fundamentals and Simulation* (Springer Science & Business Media, 2006), Vol. 29.
[12]L. Joly, C. Ybert, E. Trizac, and L. Bocquet, "Hydrodynamics within the electric double layer on slipping surfaces," Phys. Rev. Lett. **93**, 257805 (2004).
[13]L. Joly, C. Ybert, E. Trizac, and L. Bocquet, "Liquid friction on charged surfaces: From hydrodynamic slippage to electrokinetics," J. Chem. Phys. **125**, 204716 (2006).
[14]D. M. Huang, C. Cottin-Bizonne, C. Ybert, and L. Bocquet, "Aqueous electrolytes near hydrophobic surfaces: Dynamic effects of ion specificity and hydrodynamic slip," Langmuir **24**, 1442–1450 (2008).
[15]J. Smiatek, M. P. Allen, and F. Schmid, "Tunable-slip boundaries for coarse-grained simulations of fluid flow," Eur. Phys. J. E **26**, 115–122 (2008).
[16]J. Smiatek, M. Sega, C. Holm, U. D. Schiller, and F. Schmid, "Mesoscopic simulations of the counterion-induced electro-osmotic flow: A comparative study," J. Chem. Phys. **130**, 244702 (2009).
[17]D. J. Bonthuis and R. R. Netz, "Unraveling the combined effects of dielectric and viscosity profiles on surface capacitance, electro-osmotic mobility, and electric surface conductivity," Langmuir **28**, 16049–16059 (2012).
[18]Y. Uematsu, R. R. Netz, and D. J. Bonthuis, "Analytical interfacial layer model for the capacitance and electrokinetics of charged aqueous interfaces," Langmuir **34**, 9097–9113 (2018).
[19]E. F. Silkina, E. S. Asmolov, and O. I. Vinogradova, "Electro-osmotic flow in hydrophobic nanochannels," Phys. Chem. Chem. Phys. **21**, 23036–23043 (2019).
[20]P. A. Thompson and S. M. Troian, "A general boundary condition for liquid flow at solid surfaces," Nature **389**, 360–362 (1997).
[21]S. Kumar Kannam, B. D. Todd, J. S. Hansen, and P. J. Daivis, "Slip length of water on graphene: Limitations of non-equilibrium molecular dynamics simulations," J. Chem. Phys. **136**, 024705 (2012).
[22]J. N. Israelachvili, *Intermolecular and Surface Forces* (Academic Press, 2011).
[23]S. Engstrom and H. Wennerstrom, "Ion condensation on planar surfaces. A solution of the Poisson-Boltzmann equation for two parallel charged plates," J. Phys. Chem. **82**, 2711–2714 (1978).
[24]J. S. Hansen, B. D. Todd, and P. J. Daivis, "Prediction of fluid velocity slip at solid surfaces," Phys. Rev. E **84**, 016313 (2011).
[25]S. Varghese, J. S. Hansen, and B. D. Todd, "Improved methodology to compute the intrinsic friction coefficient at solid–liquid interfaces," J. Chem. Phys. **154**, 184707 (2021).
[26]H. Bruus, *Theoretical Microfluidics* (Oxford University Press, 2008), Vol. 18.
[27]W. Press, W. Vettering, S. Teukolsky, and B. Flannery, *Numerical Recipes in C* (Cambridge University Press, Cambridge, 1992).
[28]J. W. Eaton, D. Bateman, S. Hauberg, and R. Wehbring, GNU octave version 6.3.0 manual: A high-level interactive language for numerical computations, 2021.
[29]S. Plimpton, "Fast parallel algorithms for short-range molecular dynamics," J. Comput. Phys. **117**, 1–19 (1995).
[30]J.-L. Barrat and L. Bocquet, "Large slip effect at a nonwetting fluid-solid interface," Phys. Rev. Lett. **82**, 4671 (1999).
[31]S. Alosious, S. K. Kannam, S. P. Sathian, and B. D. Todd, "Prediction of Kapitza resistance at fluid-solid interfaces," J. Chem. Phys. **151**, 194502 (2019).
[32]R. Hockney and J. Eastwood, *Computer Simulations Using Particles* (McGraw-Hill, New York, 1981), Vol. 61.
[33]I.-C. Yeh and M. L. Berkowitz, "Ewald summation for systems with slab geometry," J. Chem. Phys. **111**, 3155–3162 (1999).
[34]B. D. Todd and P. J. Daivis, *Nonequilibrium Molecular Dynamics: Theory, Algorithms and Applications* (Cambridge University Press, 2017).
[35]S. Nosé, "A unified formulation of the constant temperature molecular dynamics methods," J. Chem. Phys. **81**, 511–519 (1984).
[36]W. G. Hoover, "Canonical dynamics: Equilibrium phase-space distributions," Phys. Rev. A **31**, 1695 (1985).
[37]W. C. Swope, H. C. Andersen, P. H. Berens, and K. R. Wilson, "A computer simulation method for the calculation of equilibrium constants for the formation of physical clusters of molecules: Application to small water clusters," J. Chem. Phys. **76**, 637–649 (1982).
[38]Y. Xie, L. Fu, T. Niehaus, and L. Joly, "Liquid-solid slip on charged walls: The dramatic impact of charge distribution," Phys. Rev. Lett. **125**, 014501 (2020).
[39]B. D. Todd and J. S. Hansen, "Nonlocal viscous transport and the effect on fluid stress," Phys. Rev. E **78**, 051202 (2008).
[40]S. L. Barker, D. Ross, M. J. Tarlov, M. Gaitan, and L. E. Locascio, "Control of flow direction in microfluidic devices with polyelectrolyte multilayers," Anal. Chem. **72**, 5925–5929 (2000).
[41]V. Sénéchal, H. Saadaoui, J. Rodriguez-Hernandez, and C. Drummond, "Electrowetting of weak polyelectrolyte-coated surfaces," Langmuir **33**, 4996–5005 (2017).
[42]D. J. Bonthuis and R. R. Netz, "Beyond the continuum: How molecular solvent structure affects electrostatics and hydrodynamics at solid–electrolyte interfaces," J. Phys. Chem. B **117**, 11397–11413 (2013).
[43]D. J. Bonthuis, S. Gekle, and R. R. Netz, "Profile of the static permittivity tensor of water at interfaces: Consequences for capacitance, hydration interaction and ion adsorption," Langmuir **28**, 7679–7694 (2012).
[44]S. Varghese, S. K. Kannam, J. S. Hansen, and S. P. Sathian, "Effect of hydrogen bonds on the dielectric properties of interfacial water," Langmuir **35**, 8159–8166 (2019).